

University of Groningen

## Giant magnon spin conductivity in ultrathin yttrium iron garnet films

Wei, X. Y.; Santos, O. Alves; Lusero, C. H. Sumba; Bauer, G. E.W.; Ben Youssef, J.; van Wees, B. J.

*Published in:*  
 Nature Materials

*DOI:*  
[10.1038/s41563-022-01369-0](https://doi.org/10.1038/s41563-022-01369-0)

**IMPORTANT NOTE:** You are advised to consult the publisher's version (publisher's PDF) if you wish to cite from it. Please check the document version below.

*Document Version*  
 Publisher's PDF, also known as Version of record

*Publication date:*  
 2022

[Link to publication in University of Groningen/UMCG research database](#)

*Citation for published version (APA):*

Wei, X. Y., Santos, O. A., Lusero, C. H. S., Bauer, G. E. W., Ben Youssef, J., & van Wees, B. J. (2022). Giant magnon spin conductivity in ultrathin yttrium iron garnet films. *Nature Materials*, 21(12), 1352-1356. <https://doi.org/10.1038/s41563-022-01369-0>

### Copyright

Other than for strictly personal use, it is not permitted to download or to forward/distribute the text or part of it without the consent of the author(s) and/or copyright holder(s), unless the work is under an open content license (like Creative Commons).

The publication may also be distributed here under the terms of Article 25fa of the Dutch Copyright Act, indicated by the "Taverne" license. More information can be found on the University of Groningen website: <https://www.rug.nl/library/open-access/self-archiving-pure/taverne-amendment>.

### Take-down policy

If you believe that this document breaches copyright please contact us providing details, and we will remove access to the work immediately and investigate your claim.

*Downloaded from the University of Groningen/UMCG research database (Pure): <http://www.rug.nl/research/portal>. For technical reasons the number of authors shown on this cover page is limited to 10 maximum.*



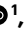

# Giant magnon spin conductivity in ultrathin yttrium iron garnet films

Received: 30 December 2021

Accepted: 16 August 2022

Published online: 22 September 2022

 Check for updates

X.-Y. Wei <sup>1</sup>✉, O. Alves Santos <sup>1</sup>, C. H. Sumba Lusero <sup>1</sup>, G. E. W. Bauer <sup>1,2,3</sup>, J. Ben Youssef<sup>4</sup> and B. J. van Wees<sup>1</sup>

Conductivities are key material parameters that govern various types of transport (electronic charge, spin, heat and so on) driven by thermodynamic forces. Magnons, the elementary excitations of the magnetic order, flow under the gradient of a magnon chemical potential<sup>1–3</sup> in proportion to a magnon (spin) conductivity. The magnetic insulator yttrium iron garnet is the material of choice for efficient magnon spin transport. Here we report a giant magnon conductivity in thin yttrium iron garnet films with thicknesses down to 3.7 nm when the number of occupied two-dimensional subbands is reduced from a large number to a few, which corresponds to a transition from three-dimensional to two-dimensional magnon transport. We extract a two-dimensional magnon spin conductivity around 1 S at room temperature, comparable to the (electronic) conductivity of the high-mobility two-dimensional electron gas in GaAs quantum wells at millikelvin temperatures<sup>4</sup>. Such high conductivities offer opportunities to develop low-dissipation magnon-based spintronic devices.

The spin current density  $j_s$  in metals is the difference between the up-spin  $j_\uparrow$  and down-spin  $j_\downarrow$  charge current densities measured in amperes per square metre, which is driven by a gradient of the spin chemical potential (often called spin accumulation)  $\mu_s$ . The spin conductivity  $\sigma_s$ , defined as  $j_s = j_\uparrow - j_\downarrow = \sigma_s \partial \mu_s / e$ , can be expressed in electrical units as siemens per metre;  $e$  is the electron charge. In magnetic insulators, charge currents are absent, but each magnon carries angular momentum  $\hbar$ , where  $\hbar$  is the reduced Planck constant, which is equivalent to the spin current in metals carried by a pair of spin-up ( $+\hbar/2$ ) and spin-down ( $-\hbar/2$ ) electrons that flow in opposite directions.

A magnon current  $j_m$  can be defined as the magnon number current times electron charge  $e$ . In magnetic-insulator-based spintronic devices, magnon spin currents are injected, detected and modulated by microwave striplines or electric contacts made from a heavy metal for charge–spin conversion<sup>5–9</sup>. The corresponding transport parameter is the magnon conductivity  $\sigma_m$ , i.e. the magnon current density divided by the gradient of its chemical potential. The unit of the magnon conductivity in  $j_m = \sigma_m \partial \mu_m / e$ , where  $\mu_m$  is the magnon chemical potential, is then the same as that of electrons in a metal<sup>1</sup>. The value of  $\sigma_m = 4 \times 10^5 \text{ S m}^{-1}$

in a 210-nm-thick yttrium iron garnet (YIG) film at room temperature<sup>6</sup> corresponds to the electronic conductivity of bad metals.

The high magnetic and acoustic quality of magnetic insulators make them the ideal material for all-magnon logical circuits and magnon-based quantum information<sup>10</sup>. An example of recent progress in magnon-based computing is an integrated magnonic half-adder based on 350-nm-wide wave guides made from 85-nm-thick YIG films<sup>11</sup>. However, these devices operate with coherent magnons (on the scale of gigahertz) excited by narrow microwave striplines which can not be integrated into an all-electrical circuit. Therefore, it is attractive to inject magnons electrically<sup>12</sup>. Incoherent thermal magnons with energies up to the thermal energy at room temperature (several terahertz) carry the electrically injected spin current. Also, scalability to smaller structure sizes, essential for future high-performance processing units, requires micro- and nanofabrication in all dimensions.

The first step is the growth of films of a few or even a single unit cell. Previously, magnon transport was reported in transistor structures on films down to about 10 nm, which shows that ultrathin films can maintain high quality and display intriguing nonlinear magnon

<sup>1</sup>Physics of Nanodevices, Zernike Institute for Advanced Materials, University of Groningen, Groningen, the Netherlands. <sup>2</sup>WPI-AIMR, Institute for Materials Research, CSRN, Tohoku University, Sendai, Japan. <sup>3</sup>Kavli Institute for Theoretical Sciences, University of the Chinese Academy of Sciences, Beijing, China. <sup>4</sup>Lab-STICC, CNRS, Université de Bretagne Occidentale, Brest, France. ✉e-mail: [x.wei@rug.nl](mailto:x.wei@rug.nl)

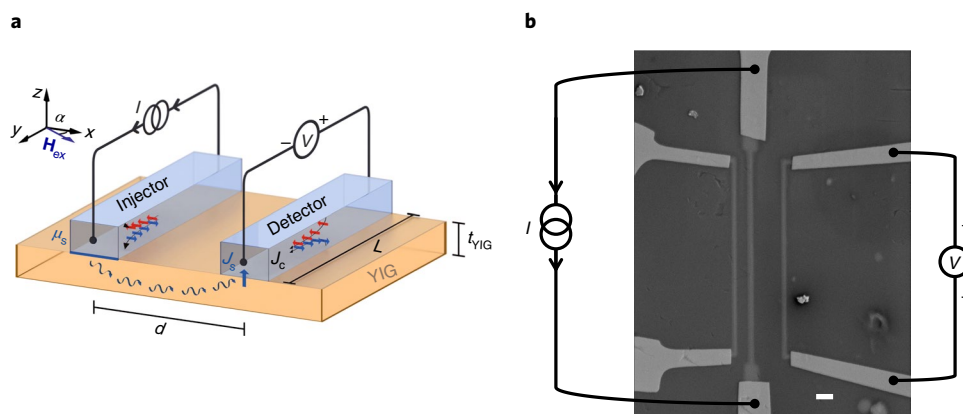


**Fig. 1 | Device layout.** **a**, Schematic representation of the experimental geometry. Two Pt strips deposited on top of YIG serve as the magnon detector and injector via the direct and inverse spin Hall effect. A low-frequency a.c. current with a r.m.s. value of  $I$  through the left Pt strip injects magnons. The centre-to-centre distance of the injector and the detector is  $d$  and the length of the injector/detector is  $L$ . A spin accumulation  $\mu_s$  is formed at the Pt/YIG interface due to the SHE when a charge current passes through the injector and excites a magnon non-equilibrium underneath the injector. The diffusive magnons are absorbed

at the drain, which induces a spin current density  $j_s$ . Then,  $j_s$  is converted into a charge current density  $j_c$  due to ISHE. Using a lock-in technique, the first harmonic voltage is measured simultaneously by the right Pt strip, that is, a magnon detector;  $\alpha$  is the angle of the external magnetic field  $\mathbf{H}_{\text{ex}}$ . **b**, Scanning electron microscopy image of the geometry. The parallel vertical lines are the platinum injector and detector, and they are contacted by gold leads. Current and voltage connections are indicated schematically. The scale bar represents 2  $\mu\text{m}$ .

effects<sup>13,14</sup>. However, the scattering by surface roughness is expected to increase in even thinner films<sup>15</sup>. This could be an obstacle for magnon spin transport in ultrathin YIG films as it hinders observation of a transition from a three-dimensional to a two-dimensional magnon gas when the thermal wavelength  $\lambda_{\text{thermal}} = \sqrt{4\pi\hbar\gamma D/(k_B T)}$  ( $\sim 2$  nm at room temperature) approaches the film thickness  $t_{\text{YIG}}$ , where  $\gamma$  is the gyromagnetic ratio,  $D$  is the spin wave stiffness,  $T$  is the temperature and  $k_B$  is the Boltzmann constant.

Here we report measurements of the magnon conductivity of YIG films with thicknesses down to 3.7 nm. Much to our surprise, the magnon transport turns out to be strongly enhanced in the ultrathin regime. We report a drastical increase in magnon conductivity of up to  $\sigma_m = 1.6 \times 10^8 \text{ S m}^{-1}$  at room temperature, which even exceeds the electronic spin conductivity of high-purity copper. This increase is intimately connected to the small number of occupied subbands and apparent domination by the lowest subband in our films. These results can importantly boost the performance of magnon-based information technology<sup>10,16</sup>.

We employ a non-local configuration<sup>6</sup> (Fig. 1a) of two Pt thin film strips with length  $L$  at a distance  $d$  on top of YIG films grown on gallium gadolinium garnet by liquid-phase epitaxy. An electric charge current  $I$  through the injector generates a transverse spin current due to the spin Hall effect (SHE)<sup>17</sup>, resulting in a spin accumulation  $\mu_s$  in Pt at the interface to YIG. The injector-conversion coefficient  $\eta_{\text{inj}} = \mu_s/(eI)$  depends on the properties and dimensions of the Pt strip as explained in Supplementary Section I. The effective interface spin conductance results from the exchange interaction across the interface and produces a magnon chemical potential  $\mu_m$  on the YIG side of the interface that acts as a magnon source, where  $\mu_m \approx \mu_s$  since the interface spin resistance can be ignored (Supplementary Section III). The detector electrode is a magnon drain that absorbs magnons and converts them into a spin current  $j_s$  entering the Pt detector electrode ( $j_s^{\text{det}}$ ). The inverse spin Hall effect (ISHE) generates a non-local (nl) voltage  $V_{\text{nl}}$  at the detector with conversion coefficient  $\eta_{\text{det}} = V_{\text{nl}}/j_s^{\text{det}}$ . By reciprocity,  $\eta_{\text{inj}} = \eta_{\text{det}}$  when injector and detector contacts have the same properties (Supplementary Section I for details). Since the signal scales with  $L$ , a normalized non-local resistance can be defined as  $R_{\text{nl}} = V_{\text{nl}}/(IL)$ . The magnon conductance follows from the measured non-local resistance:

$$G_m = \frac{1}{\eta_{\text{inj}}\eta_{\text{det}}} \frac{V_{\text{nl}}}{I} = \frac{R_{\text{nl}}L}{\eta_{\text{inj}}\eta_{\text{det}}}. \quad (1)$$

The magnon conductivity  $\sigma_m$  as a function of the thickness  $t_{\text{YIG}}$  of the YIG films in Fig. 1 then follows from the magnon spin conductance:

$$\sigma_m = \frac{G_m d}{t_{\text{YIG}} L}. \quad (2)$$

For the films with  $t_{\text{YIG}}$  much smaller than the magnon relaxation length  $\lambda_m$  as well as the lateral device dimension,  $\mu_m$  can be considered constant in the  $z$  direction. Therefore, we use the following equation to describe magnon diffusion<sup>6,18</sup>:

$$R_{\text{nl}} = \frac{\sigma_m t_{\text{YIG}} \eta_{\text{inj}} \eta_{\text{det}}}{\lambda_m} \text{csch} \frac{d}{\lambda_m} \rightarrow \begin{cases} \frac{\sigma_m t_{\text{YIG}} \eta_{\text{inj}} \eta_{\text{det}}}{d} & d \ll \lambda_m \\ \frac{2\sigma_m t_{\text{YIG}} \eta_{\text{inj}} \eta_{\text{det}}}{\lambda_m} \exp(-\frac{d}{\lambda_m}) & d \gg \lambda_m \end{cases} \quad (3)$$

When the spacing  $d$  is smaller than  $\lambda_m$ , it is the ohmic regime in which the magnons are conserved,  $R_{\text{nl}}(G_m) \propto d^{-1}$ . Otherwise, the signal decays exponentially as a function of distance due to magnon relaxation.

We measure  $R_{\text{nl}}$  at room temperature as a function of an external in-plane magnetic field  $\mathbf{H}_{\text{ex}}$  with  $|\mathbf{H}_{\text{ex}}| = 50$  mT, which we rotate in the plane (Fig. 1a). We modulate the current  $I$  by a low frequency ( $\omega/2\pi = 18$  Hz) and detect the first and second harmonic signals,  $V_{\text{nl}}(\omega)$  and  $V_{\text{nl}}(2\omega)$ , respectively, by lock-in amplifier (Methods).  $V_{\text{nl}}(2\omega)$  depends on the spin Seebeck generation and diffusion of magnons under an inhomogeneous temperature profile, which renders interpretation difficult<sup>19,20</sup> (Supplementary Section V). Therefore, we focus on  $V_{\text{nl}}(\omega)$ , from which we can extract the normalized non-local resistance  $R_{\text{nl}}^{\omega}$ ,

$$\frac{V_{\text{nl}}(\omega)}{IL} = R_{\text{nl}}^{\omega} \cos^2 \alpha + R_0^{\omega}, \quad (4)$$

where  $R_0^{\omega}$  is an offset resistance (Methods) and  $\alpha$  is the angle between  $\mathbf{H}_{\text{ex}}$  and the  $x$  axis. In Fig. 2, the angle-dependent measurements in YIG films of various thickness show that  $R_{\text{nl}}^{\omega}$  becomes four times larger when the film is over fifty times thinner, from 210 nm to 3.7 nm. We also observe a strongly increased non-local signal in ultrathin films in Fig. 3 as a function of contact separation for a wide range of  $t_{\text{YIG}}$  values including results on ultrathin YIG films for 400-nm-wide Pt strips and

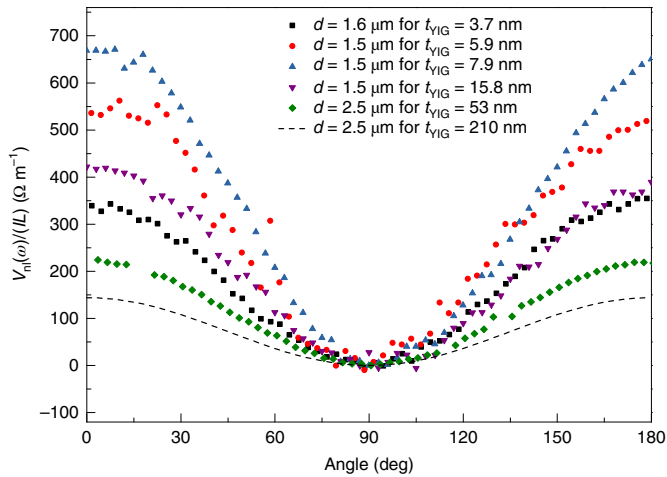


**Fig. 2 | Angular dependence of the normalized non-local signal  $\frac{V_{nl}(\omega)}{IL}$ .** Dependence of the normalized non-local signal  $\frac{V_{nl}(\omega)}{IL}$  on the magnetization direction of YIG films for a short centre-to-centre distance between the injector and the detector. The offset  $R_0^{1\omega}$  in Eq. (4) has been subtracted. The corresponding non-local resistance  $R_{nl}^{1\omega}$  strongly increases with decreasing thickness. The dashed line is the thick-film reference from Cornelissen et al.<sup>6</sup>

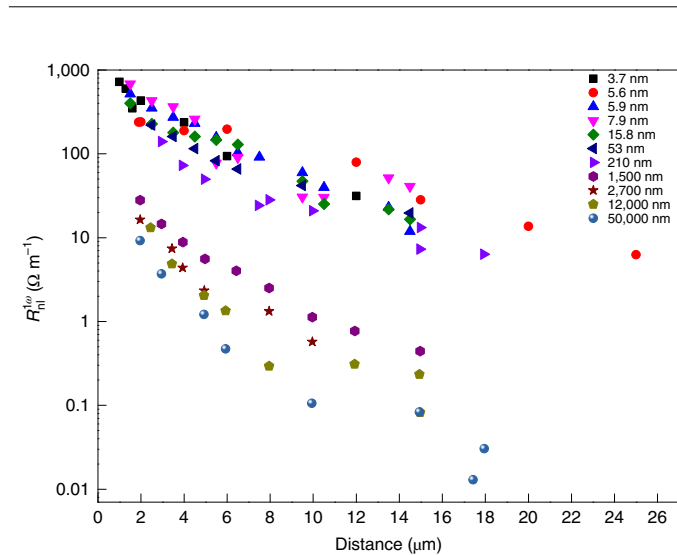


**Fig. 3 | Distance dependence of the non-local resistance  $R_{nl}^{1\omega}$ .** Non-local resistance  $R_{nl}^{1\omega}$  as a function of injector–detector distance of the samples in series A and with  $t_{YIG}$  varying from 3.7 nm to 5  $\mu\text{m}$ . The width of the injector–detector distance is 400 nm. The results for  $t_{YIG} \geq 210$  nm are adopted from Cornelissen et al.<sup>6</sup> and Shan et al.<sup>21</sup>

for thicker films ( $t_{YIG} \geq 210$  nm; refs.<sup>6,21</sup>). Figure 4a emphasizes the dramatic enhancement of  $R_{nl}^{1\omega}$  for the thinnest films down to  $t_{YIG} = 3.7$  nm and fixed  $d = 2.5$   $\mu\text{m}$ , which can be attributed to the  $t_{YIG}$  dependence of  $\sigma_m$  because  $\lambda_m > 2.5$   $\mu\text{m}$  for all thicknesses (Supplementary Section IV for details). The  $R_{nl}^{1\omega}$  value increases with decreasing thickness and saturates for both the thinnest and thickest films.

A finite-element model<sup>1</sup> can simulate the depth ( $z$ ) dependence of  $\mu_m$  when  $t_{YIG} > \lambda_m$  (Supplementary Section I for details). This leads to a limiting  $\sigma_m \rightarrow 3 \times 10^8$   $\text{S m}^{-1}$  in Fig. 4b for thicker films, which represents the bulk value. The simulated  $R_{nl}$  values for  $d = 2.5$   $\mu\text{m}$  in Fig. 4c have been fitted to  $R_{nl}^{1\omega}$  in Fig. 4a by conductivities that are strongly enhanced in the regime  $t_{YIG} < \lambda_m$ . For  $t_{YIG} = 3.7$  nm, the magnon conductivity  $\sigma_m = 1.6 \times 10^8$   $\text{S m}^{-1}$  is four orders of magnitude larger than the bulk

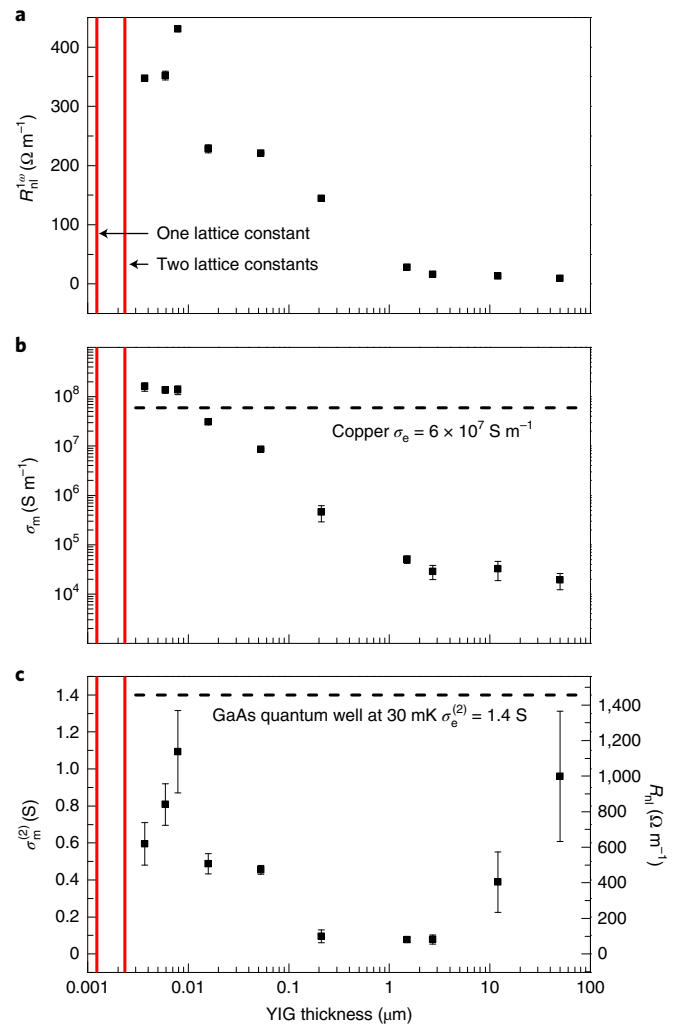


**Fig. 4 | Thickness dependence of the non-local magnon transport.** **a**, The non-local resistance  $R_{nl}^{1\omega}$  for  $d = 2.5$   $\mu\text{m}$  as a function of  $t_{YIG}$  obtained by extraction by fitting the angle-dependent non-local resistance to Eq. (4). The error bars represent the standard statistical error from the least-squares analysis. The results for  $t_{YIG} \geq 210$  nm are adopted from Cornelissen et al.<sup>6</sup> and Shan et al.<sup>21</sup> **b**, Thickness dependence of the magnon conductivity  $\sigma_m$  obtained by the best fit for different distances with statistical error bars. **c**, Thickness dependence of the two-dimensional magnon spin conductivity  $\sigma_m^{(2)}$  and the non-local resistance  $R_{nl}^{1\omega}$  from the simulation, with values based on the best fit for the magnon conductivity. The saturation at  $t_{YIG} \rightarrow 0$  indicates that the film approaches the two-dimensional regime in the ultrathin limit. The obtained error bars in **b** and **c** indicate the scatter in the best fits by the numerical simulations (Supplementary Section II).

value, exceeding the electronic conductivity  $\sigma_e$  of pure metals such as copper with  $\sigma_e = 6 \times 10^7$   $\text{S m}^{-1}$  (ref.<sup>22</sup>). The observed saturation at  $t_{YIG} \rightarrow 0$  appears to reflect an increased role of surface roughness scattering that we do not model explicitly.

The  $\sigma_m$  and  $\sigma_e$  above are conductivities in three dimensions. To distinguish the conductivity in  $v$  dimensions ( $v = 2, 3$ ), the conductivities now are labeled with  $v$ ,  $\sigma_m^{(v)}$  and  $\sigma_e^{(v)}$ , where  $\sigma_m^{(3)} = \sigma_m$  and  $\sigma_e^{(3)} = \sigma_e$ .

A magnon conductivity that diverges for  $t_{YIG} \rightarrow 0$ , such as  $\sigma_m^{(3)} \approx \sigma_m^{(2)}/t_{YIG}$  simply suggests two-dimensional transport. In Fig. 4c,  $\sigma_m^{(2)}$  has a local maximum at  $t_{YIG} = 7.9$  nm. The decrease for the thinnest layers is not statistically relevant, however. Within this uncertainty, magnon transport approaches the two-dimensional limit in ultrathin YIG films, with

a limiting  $\sigma_m^{(2)}$  for  $t_{\text{YIG}} < 10$  nm; that is higher two-dimensional subbands do not contribute notably even though they are still populated (as discussed below). The two-dimensional subbands correspond to magnon modes that propagate in-plane but with confined out-of-plane dynamics in the form of perpendicular standing spin waves. Extrapolation to zero thickness leads to  $\sigma_m^{(2)} \approx 1$  S. This value at room temperature is comparable to that of the high-mobility two-dimensional electron gas at millikelvin temperatures, where the two-dimensional electronic conductivity  $\sigma_e^{(2)}$  is around 1.4 S in GaAs quantum wells<sup>4</sup>.

The magnons propagate in the plane with wave vector  $\mathbf{k}$  and form perpendicular standing spin waves in the  $z$  direction labelled by an integer  $n$ . The exchange interaction scales like  $-k^2$  and dominates the magnon dispersion  $\varepsilon_{nk}$  at thermal energies ( $-k_B T$ ) with small magneto-dipolar corrections. A magnon with energy  $\varepsilon_{nk} = \hbar\gamma D(k^2 + (n\pi/t_{\text{YIG}})^2)$  contributes to the conduction proportional to its thermal occupation  $N_{nk} = 1/\{\exp[\varepsilon_{nk}/(k_B T)] - 1\}$ . For YIG,  $\gamma/2\pi = 28$  GHz  $T^{-1}$  and the spin wave stiffness<sup>23</sup>  $D = 5 \times 10^{-17}$  T  $m^2$ . We define the highest occupied subband  $n$  as

$$n = \text{int}\left(\frac{t_{\text{YIG}}}{\pi} \sqrt{\frac{k_B T}{\hbar\gamma D}}\right) \quad (5)$$

at  $\varepsilon_{n0} < k_B T$  as a function of thickness<sup>24</sup>, where  $\text{int}(x)$  is the largest integer no more than  $x$ . For  $t_{\text{YIG}} = 3.7$  nm, only three approximately two-dimensional subbands are occupied at room temperature.

The simplest model for the magnon conductivity in  $v$  dimensions ( $v = 2, 3$ ) follows from the Boltzmann equation with a constant relaxation time  $\tau$ :

$$\sigma_m^{(v)} = \frac{e^2 \tau^{(v)}}{k_B T} \int \frac{d\mathbf{k}}{(2\pi)^v} \left(\frac{\partial \varepsilon_{\mathbf{k}}}{\hbar \partial k_z}\right)^2 \frac{e^{\varepsilon_{\mathbf{k}}/(k_B T)}}{(e^{\varepsilon_{\mathbf{k}}/(k_B T)} - 1)^2} \quad (6)$$

where  $\varepsilon_{\mathbf{k}} = \hbar\gamma D k^2$ . Magnetic freeze-out experiments show that the contributions from the low-frequency magnons (on the scale of gigahertz) are notable even at room temperature, presumably reflecting low mobilities of thermal exchange magnons<sup>25–27</sup>. This can be represented by a high-momentum cut-off  $K_\infty \approx 1$  nm<sup>-1</sup> at magnon frequencies  $\varepsilon_\infty/\hbar$  on the scale of terahertz. In the high-temperature limit  $k_B T \gg \varepsilon_k$ , the conductivities do not depend on  $\gamma D$ :

$$\sigma_m^{(3)} = \frac{2e^2 k_B T \tau^{(3)}}{3\hbar^2 \pi^2} K_\infty, \quad (7)$$

$$\sigma_m^{(2)} = \frac{e^2 k_B T \tau^{(2)}}{\pi \hbar^2} \log \frac{K_\infty}{K_0}, \quad (8)$$

where  $K_0$  is a low-momentum cutoff by the magnon gap of  $\varepsilon_0/\hbar$ , which is on the scale of gigahertz. By comparing these equations with the experimental results  $\sigma_m^{(3)} \approx 3 \times 10^4$  S  $m^{-1}$  and the present  $\sigma_m^{(2)} \approx 1$  S and using the scattering times as adjustable parameters, we arrive at  $\tau^{(3)} \approx 40$  fs and  $\tau^{(2)} \approx 0.1$  ns. Based on a diffusion model, Fang et al.<sup>28</sup> recently predicted that the magnon mean free path should be much larger in two dimensions than in three dimensions. The short scattering time in three dimensions can be explained by highly efficient magnon-phonon scattering at room temperature<sup>1</sup>. While the high-momentum cut-off plays an important role in three dimensions, the near independence of  $\sigma_m^{(2)}$  emphasizes the importance of the near bandgap excitations for transport in two dimensions. Coherent magnons excited at gigahertz frequencies can propagate over centimetres in spite of their small group velocity because they scatter only weakly at phonons<sup>29</sup>. Their contribution has a much larger effect on transport in ultrathin films than in the bulk, which is consistent with the magnetic field and temperature dependences reported in the

Supplementary Information. The estimated scattering time of  $\tau^{(2)} = 0.1$  ns may be limited by the film roughness scattering. The precise mechanism can be elucidated only by more extensive experimental and theoretical studies of the temperature and field dependences.

While magnon-based devices do not suffer from Joule heating, magnon transport is not dissipationless<sup>6,30</sup> even for transport on length scales shorter than the magnon relaxation length, where magnons are conserved. The observed giant magnon conductivity is therefore excellent news, implying low dissipation from magnon-phonon scattering even at room temperature. Ultrathin films can therefore be driven with relative ease into the nonlinear regime in, for example, magnon spin transistors<sup>13,14</sup>, facilitating electrically induced magnon Bose-Einstein condensation and magnon spin superfluidity<sup>31,32</sup>. The robustness of the magnon mobility for thin films close to the monolayer thickness should allow magnon transport in nanostructures such as constrictions, wires and dots with feature sizes of a few nanometres without loss of magnetic functionality.

## Online content

Any methods, additional references, Nature Research reporting summaries, source data, extended data, supplementary information, acknowledgements, peer review information; details of author contributions and competing interests; and statements of data and code availability are available at <https://doi.org/10.1038/s41563-022-01369-0>.

## References

- Cornelissen, L. J., Peters, K. J. H., Bauer, G. E. W., Duine, R. A. & van Wees, B. J. Magnon spin transport driven by the magnon chemical potential in a magnetic insulator. *Phys. Rev. B* **94**, 014412 (2016).
- Chunhui, D. et al. Control and local measurement of the spin chemical potential in a magnetic insulator. *Science* **357**, 195–198 (2017).
- Olsson, K. S. et al. Pure spin current and magnon chemical potential in a nonequilibrium magnetic insulator. *Phys. Rev. X* **10**, 021029 (2020).
- Chung, Y. J. et al. Ultra-high-quality two-dimensional electron systems. *Nat. Mater.* **20**, 632–637 (2021).
- Brataas, A., van Wees, B., Klein, O., de Loubens, G. & Viret, M. Spin insulatronics. *Phys. Rep.* **885**, 1–27 (2020).
- Cornelissen, L. J., Liu, J., Duine, R. A., Ben Youssef, J. & van Wees, B. J. Long-distance transport of magnon spin information in a magnetic insulator at room temperature. *Nat. Phys.* **11**, 1022–1026 (2015).
- Lebrun, R. et al. Tunable long-distance spin transport in a crystalline antiferromagnetic iron oxide. *Nature* **561**, 222–225 (2018).
- Chumak, A. V., Serga, A. A. & Hillebrands, B. Magnon transistor for all-magnon data processing. *Nat. Commun.* **5**, 4700 (2014).
- Cornelissen, L. J., Liu, J., van Wees, B. J. & Duine, R. A. Spin-current-controlled modulation of the magnon spin conductance in a three-terminal magnon transistor. *Phys. Rev. Lett.* **120**, 097702 (2018).
- Barman, A. et al. The 2021 magnonics roadmap. *J. Phys. Condens. Matter* **33**, 413001 (2021).
- Wang, Q. et al. A magnonic directional coupler for integrated magnonic half-adders. *Nat. Electron.* **3**, 765–774 (2020).
- Althammer, M. All-electrical magnon transport experiments in magnetically ordered insulators. *Phys. Status Solidi Rapid Res. Lett.* **15**, 2100130 (2021).
- Wimmer, T. et al. Spin transport in a magnetic insulator with zero effective damping. *Phys. Rev. Lett.* **123**, 257201 (2019).
- Liu, J., Wei, X.-Y., Bauer, G. E. W., Ben Youssef, J. & van Wees, B. J. Electrically induced strong modulation of magnon transport in ultrathin magnetic insulator films. *Phys. Rev. B* **103**, 214425 (2021).

15. Yu, T., Sharma, S., Blanter, Y. M. & Bauer, G. E. W. Surface dynamics of rough magnetic films. *Phys. Rev. B* **99**, 174402 (2019).
16. Li, Y. et al. Hybrid magnonics: physics, circuits, and applications for coherent information processing. *J. Appl. Phys.* **128**, 130902 (2020).
17. Sinova, J., Valenzuela, S. O., Wunderlich, J., Back, C. H. & Jungwirth, T. Spin Hall effects. *Rev. Mod. Phys.* **87**, 1213–1260 (2015).
18. Takahashi, S. & Maekawa, S. Spin injection and detection in magnetic nanostructures. *Phys. Rev. B* **67**, 052409 (2003).
19. Uchida, K. et al. Observation of the spin Seebeck effect. *Nature* **455**, 778–781 (2008).
20. Gomez-Perez, J. M., Vélez, S., Hueso, L. E. & Casanova, F. Differences in the magnon diffusion length for electrically and thermally driven magnon currents in  $Y_3Fe_5O_{12}$ . *Phys. Rev. B* **101**, 184420 (2020).
21. Shan, J. et al. Influence of yttrium iron garnet thickness and heater opacity on the nonlocal transport of electrically and thermally excited magnons. *Phys. Rev. B* **94**, 174437 (2016).
22. Laughton, M. A. & Say, M. G. *Electrical Engineer's Reference Book* (Elsevier, 2013).
23. Klingler, S. et al. Measurements of the exchange stiffness of YIG films using broadband ferromagnetic resonance techniques. *J. Phys. D Appl. Phys.* **48**, 015001 (2014).
24. Stamps, R. & Camley, R. *Solid State Physics* Vol. 65 (Elsevier Science, 2014).
25. Kikkawa, T. et al. Critical suppression of spin Seebeck effect by magnetic fields. *Phys. Rev. B* **92**, 064413 (2015).
26. Jin, H., Boona, S. R., Yang, Z., Myers, R. C. & Heremans, J. P. Effect of the magnon dispersion on the longitudinal spin Seebeck effect in yttrium iron garnets. *Phys. Rev. B* **92**, 054436 (2015).
27. Jamison, J. S. et al. Long lifetime of thermally excited magnons in bulk yttrium iron garnet. *Phys. Rev. B* **100**, 134402 (2019).
28. Fang, H., Zhang, S. & Tserkovnyak, Y. Generalized model of magnon kinetics and subgap magnetic noise. *Phys. Rev. B* **105**, 184406 (2022).
29. Streib, S., Vidal-Silva, N., Shen, K. & Bauer, G. E. W. Magnon-phonon interactions in magnetic insulators. *Phys. Rev. B* **99**, 184442 (2019).
30. Man, H. et al. Direct observation of magnon-phonon coupling in yttrium iron garnet. *Phys. Rev. B* **96**, 100406 (2017).
31. Bender, S. A., Duine, R. A. & Tserkovnyak, Y. Electronic pumping of quasiequilibrium Bose-Einstein-condensed magnons. *Phys. Rev. Lett.* **108**, 246601 (2012).
32. Divinskiy, B. et al. Evidence for spin current driven Bose-Einstein condensation of magnons. *Nat. Commun.* **12**, 6541 (2021).

**Publisher's note** Springer Nature remains neutral with regard to jurisdictional claims in published maps and institutional affiliations.

Springer Nature or its licensor holds exclusive rights to this article under a publishing agreement with the author(s) or other rightsholder(s); author self-archiving of the accepted manuscript version of this article is solely governed by the terms of such publishing agreement and applicable law.

© The Author(s), under exclusive licence to Springer Nature Limited 2022

## Methods

### Fabrication

The YIG films are grown on  $\text{Gd}_3\text{Ga}_5\text{O}_{12}$  (gallium gadolinium garnet) substrates by liquid-phase epitaxy at the Université de Bretagne Occidentale in Brest, France, with thicknesses from 3.7 nm to 53 nm. The effective magnetization  $M_{\text{eff}}$  and the magnetic relaxation (intrinsic damping parameter  $\alpha$  and extrinsic inhomogeneous linewidth  $\Delta H_{\text{in}}$ ) are determined by broadband ferromagnetic resonance in the frequency range 2–40 GHz (Supplementary Section IV). The device patterns are written by three electron-beam lithography steps, each followed by a standard deposition and lift-off procedure. The first step produces a Ti/Au marker pattern, used to align the subsequent steps. The second step defines the platinum injector and detector strips, as deposited by d.c. sputtering in an  $\text{Ar}^+$  plasma at an argon pressure with a thickness of ~8 nm for all devices. The third step defines 5/75 nm Ti/Au leads and bonding pads, deposited by electron-beam evaporation. Devices have an injector/detector length  $L = 30/25 \mu\text{m}$ , and the strip widths  $W$  are 400 nm for series A and 100 nm for series B. The experimental results in the main text are obtained from series A. The distance-dependent non-local resistances for series B can be found in Supplementary Section III.

### Measurements

All measurements were carried out by means of three SR830 lock-in amplifiers using an excitation frequency of 18 Hz. The lock-in amplifiers are set up to measure the first and second harmonic responses of the sample. The current was sent to the sample using a custom-built current source, galvanically isolated from the rest of the measurement equipment. Voltage measurements were made using a custom-built preamplifier (gain  $10^3$ ) and amplified further using the lock-in systems. The typical excitation currents applied to the samples were 200  $\mu\text{A}$  (r.m.s.) for series A and 20  $\mu\text{A}$  for series B. The in-plane coercive field of the YIG,  $B_c$ , was below 10 mT for all YIG samples, and we applied an external field to orient the magnetization using a physical property measurement system. The samples were mounted on a rotatable sample holder with stepper motor. All experimental data in the main text were collected at 300 K (room temperature) at an applied magnetic field of 50 mT. The offset resistance  $R_0^{\text{lo}}$  arises from the spontaneous capacitive and inductive coupling between the measurement wires to and from the sample.

### Simulations

Our finite-element model implements the magnon diffusion equation in insulators in order to simulate transport of electrically injected magnons. We carried out the simulations with the COMSOL MULTIPHYSICS (v.5.4) software package, with technical details in Supplementary Section I.

## Data availability

The data of the article and Supplementary Information are available from the corresponding author upon reasonable request.

## Code availability

Numerical simulations in this work are performed using the commercial finite-element software COMSOL MULTIPHYSICS (v.5.4). All related codes are available from the corresponding author upon reasonable request.

## Acknowledgements

We thank O. Klein for insightful discussions. We also acknowledge the helpful discussion with J. Shan and T. Yu. We acknowledge the technical support from J. G. Holstein, H. de Vries, H. Adema, T. Schouten and A. Joshua. X.-Y.W. and B.J.v.W. acknowledge the support from the research programme 'Skyrmionics' (project no. 170), which is financed by the Dutch Research Council (NWO). X.-Y.W., O.A.S., C.H.S.L. and B.J.v.W. also acknowledge the support by NanoLab NL and the Spinoza Prize awarded in 2016 to B.J.v.W. by NWO. G.E.W.B. was supported by JSPS Kakenhi grant 19H00645.

## Author contributions

B.J.v.W. and X.-Y.W. conceived the experiments. X.-Y.W. designed and carried out the experiments, with help from O.A.S.; J.B.Y. supplied the YIG samples used in the fabrication of devices. X.-Y.W., O.A.S., C.H.S.L., G.E.W.B. and B.J.v.W. were involved in the analysis. X.-Y.W. wrote the paper with O.A.S., G.E.W.B. and B.J.v.W. All authors commented on the manuscript.

## Competing interests

The authors declare no competing interests.

## Additional information

**Supplementary information** The online version contains supplementary material available at <https://doi.org/10.1038/s41563-022-01369-0>.

**Correspondence and requests for materials** should be addressed to X.-Y. Wei.

**Peer review information** *Nature Materials* thanks the anonymous reviewers for their contribution to the peer review of this work.

**Reprints and permissions information** is available at [www.nature.com/reprints](http://www.nature.com/reprints).